

# Marginal Fermi Liquid behaviour from charge density fluctuations in cuprates

G. Seibold<sup>1</sup>, R. Arpaia<sup>2,3</sup>, Y. Y. Peng<sup>2,†</sup>, R. Fumagalli<sup>2</sup>, L. Braicovich<sup>2,4</sup>,  
C. Di Castro<sup>5</sup>, M. Grilli<sup>5,6,\*</sup>, G. Ghiringhelli<sup>2,7</sup>, and S. Caprara<sup>5,6,\*</sup>

<sup>1</sup> Institut für Physik, BTU Cottbus-Senftenberg - PBox 101344, D-03013 Cottbus, Germany

<sup>2</sup> Dipartimento di Fisica, Politecnico di Milano, Piazza Leonardo da Vinci 32, I-20133 Milano, Italy

<sup>3</sup> Quantum Device Physics Laboratory, Department of Microtechnology and Nanoscience,  
Chalmers University of Technology, SE-41296 Göteborg, Sweden

<sup>4</sup> ESRF, The European Synchrotron, 71 Avenue des Martyrs, F-38043 Grenoble, France

<sup>5</sup> Dipartimento di Fisica, Università di Roma “La Sapienza”, P. le Aldo Moro 5, I-00185 Roma, Italy

<sup>6</sup> CNR-ISC, via dei Taurini 19, I-00185 Roma, Italy

<sup>7</sup> CNR-SPIN, Dipartimento di Fisica, Politecnico di Milano,  
Piazza Leonardo da Vinci 32, I-20133 Milano, Italy

<sup>†</sup> Present address: Department of Physics and Seitz Materials

Research Laboratory, University of Illinois, IL-61801 Urbana, USA

\*Corresponding authors. E-mail: marco.grilli@roma1.infn.it sergio.caprara@roma1.infn.it

Besides the mechanism responsible for high critical temperature superconductivity, the grand unresolved issue of the cuprates is the occurrence of a “strange” metallic state above the so-called pseudogap temperature  $T^*$ . Even though such state has been successfully described within a phenomenological scheme, the so-called Marginal Fermi Liquid (MFL) theory [1], a microscopic explanation is still missing. However, recent resonant inelastic X-ray scattering experiments on  $\text{Nd}_{1+x}\text{Ba}_{2-x}\text{Cu}_3\text{O}_{7-\delta}$  and  $\text{YBa}_2\text{Cu}_3\text{O}_{7-\delta}$  films identified a new class of charge density fluctuations (CDFs) characterized by low characteristic energies and very short correlation lengths [2]. These CDFs are present over a very wide region of the temperature-vs-doping phase diagram and extend well above  $T^*$ . We investigated the consequences of CDFs on the electronic and transport properties and found that they can be used to explain the MFL phenomenology. Therefore, charge density fluctuations are likely the long-sought microscopic mechanism underlying the peculiarities of the normal state of cuprates.

Among the different phases and orders populating the phase diagram of superconducting cuprates, the region where the Marginal Fermi Liquid (MFL) anomalous behaviour [1] takes place has a preeminent role for this class of compounds over a rather wide doping range pivoting around optimal doping (see Fig. 1). Experimentally, the most evident benchmark of this region is represented by the linear behaviour of the electrical resistivity  $\rho(T)$  as a function of temperature, from above a doping-dependent pseudogap crossover temperature  $T^*$  up to the highest attained temperatures. Such occurrence is less evident in the underdoped regime, where  $T^*$  is almost as high as room temperature (e.g., at  $p \approx 0.11$ , see Fig. 1), while it dominates the transport properties of the normal state in its entirety around optimal doping ( $p \approx 0.17 - 0.20$ , see Fig. 1), where  $T^*$  decreases and merges with the superconducting critical temperature  $T_c$ . Beyond such occurrence, the main deviations from the paradigmatic behaviour dictated by the Landau Fermi-liquid theory of standard metals are the optical conductivity, following a non-Drude-like frequency dependence  $\sigma(\omega) \sim 1/\omega$ , and the Raman scattering intensity, starting linearly in frequency and then saturating into a flat electronic continuum, as expressed by the dependence of the charge susceptibility,  $\text{Im } \chi(\omega) \sim \omega/\max(T, |\omega|)$ .

MFL theory is based on low-energy excitations, mediating a momentum-independent electron-electron effective interaction, giving rise to a linear dependence of the imaginary part of the electron self-energy both in fre-

quency and temperature

$$\text{Im } \Sigma(\mathbf{k}, \omega) \sim \max(T, |\omega|). \quad (1)$$

A huge effort has been devoted along the years to identify these excitations, mostly based on the idea of proximity to some form of order: circulating currents [4], spin [5, 6], or charge order [7–10], the phenomenological coupling to incoherent fermions [11]. However, the observation of circulating currents is as yet rather controversial, and finite-momentum spin and charge density waves fail to mediate a momentum-independent effective interaction.

A step forward in the identification of low-energy excitations that might be responsible for the MFL behaviour was recently taken by means of resonant X-ray scattering (RXS), performed on  $\text{Nd}_{1+x}\text{Ba}_{2-x}\text{Cu}_3\text{O}_{7-\delta}$  (NBCO) and  $\text{YBa}_2\text{Cu}_3\text{O}_{7-\delta}$  (YBCO) thin films [2]. These experiments not only confirmed the occurrence of incommensurate charge density waves (CDWs), correlated over several lattice spacings, in the underdoped region and below  $T^*$  [12–20], but, quite remarkably, also identified a much larger amount of very short-ranged (2-3 lattice spacings) dynamical CDFs (see Fig. 1). These CDFs are peaked at a wavevector, along the (1,0) (0,1) directions, which is very close to that of the intermediate-range CDWs, but - differently from those - are quite robust both in temperature (they survive essentially unaltered up to the highest explored temperatures,  $T \approx 270$  K) and doping. These excitations are at low energy ( $\approx 15$  meV in an optimally doped sample with  $T_c = 93$  K) and so short ranged that

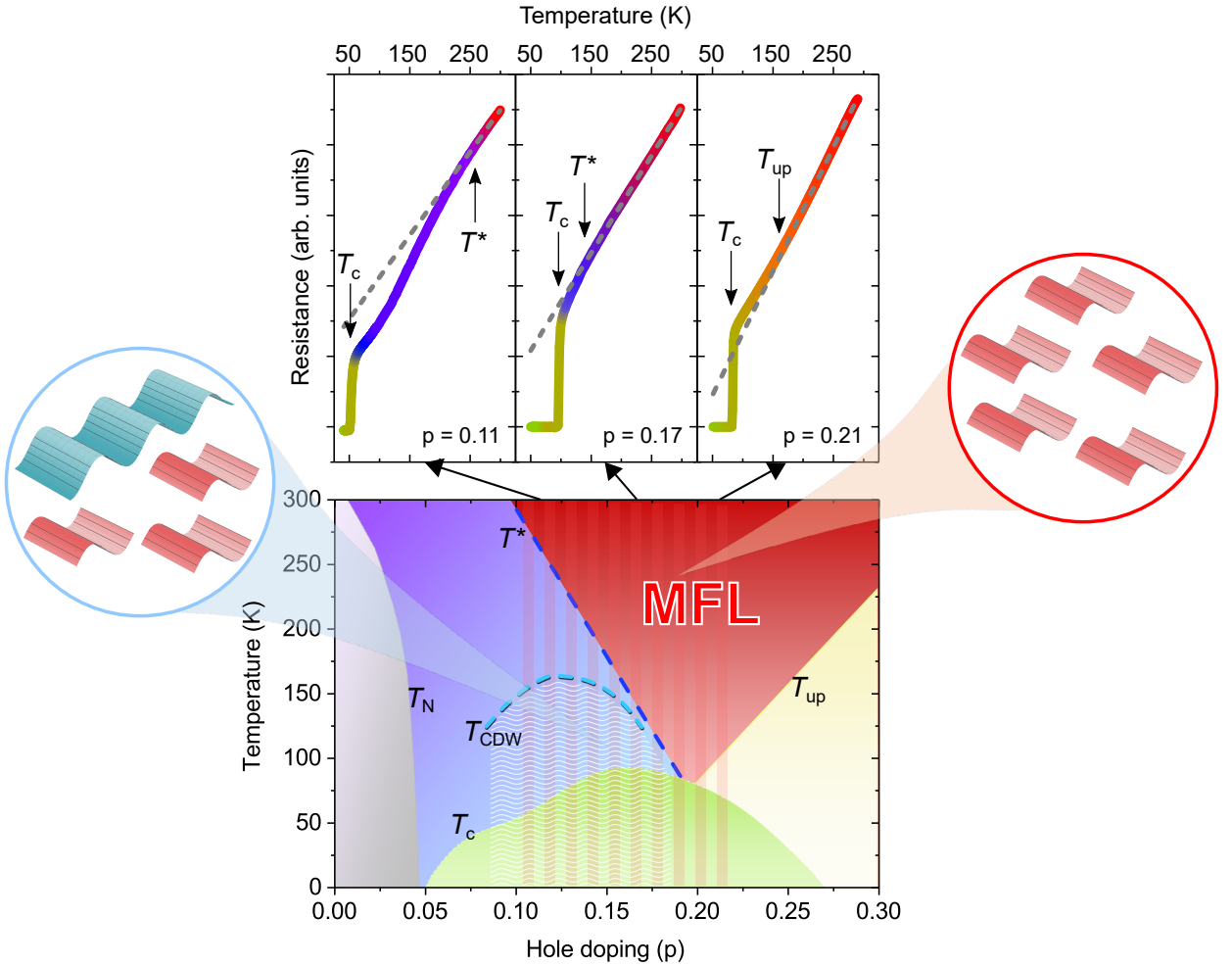


FIG. 1. Temperature-doping phase diagram of the superconducting cuprates. The region of the Marginal Fermi liquid, encompassed between the pseudogap temperature  $T^*$  and the upturn temperature  $T_{\text{up}}$  of the resistance, has a leading role in determining the properties of these compounds above the superconducting critical temperature  $T_c$ , in particular close to the optimally doped regime (e.g., at  $p \approx 0.17$ ). Above  $T^*$  and  $T_{\text{up}}$  (red region), the MFL behaviour is revealed in the experimental resistance  $R$  data by the presence of a linear temperature dependence, displayed as a red thick solid line in the  $R(T)$  curves above the phase diagram. In the underdoped regime (e.g., at  $p \approx 0.11$ ), below  $T^*$  (blue region) a downturn from the linear-in- $T$  resistance is observed, since additional mechanisms lead to deviations from the MFL regime. In the overdoped regime (e.g., at  $p \approx 0.21$ ), below  $T_{\text{up}}$  (yellow region) an upturn from the linear-in- $T$  resistance is instead observed, which is due to the setting in of the Fermi-liquid regime. Recent RXS experiments [2] showed that also the charge order phenomenon is widespread in the phase diagram. In particular, short-ranged dynamical CDFs (sketched by red waves in the circular panel on the right, and observed in the striped area) populate the MFL region, while in the underdoped region, below the onset temperature  $T_{\text{CDW}}$ , they coexist with the usual longer-ranged slower CDWs (sketched by blue waves in the circular panel on the left, and observed in the wavy area).  $T_N$  is the Néel temperature. The  $R(T)$  curves are adapted from [2, 3].

in reciprocal space they produce a very broad peak in the RXS scans. CDFs not only provide a strong scattering channel for the electrons, but all states on the Fermi surface are nearly equally affected, resulting in an essentially isotropic scattering rate [see Fig. 2(a)]. This isotropy is a distinguished feature of the MFL state.

### MFL behavior of the electron self-energy

Figure 2(a) shows a qualitative explanation of the inherent isotropy of the scattering by CDFs: despite a well defined incommensurate wave vector the overlap of the

Fermi surface with its translated and broadened replicas is almost uniform, and no particular nesting condition is needed, contrary to the CDWs where the scattering is peaked at the so-called hot spots [see fig. 2(a), right panel]. In a quantitative way, this is shown in Figure 2(b), where the actual scattering rate along the Fermi surface has been computed. This feature makes these CDFs an appealing candidate to mediate the isotropic scattering required by the MFL theory. We therefore test this expectation by explicitly calculating how the CDFs dress the electron quasiparticles modifying their

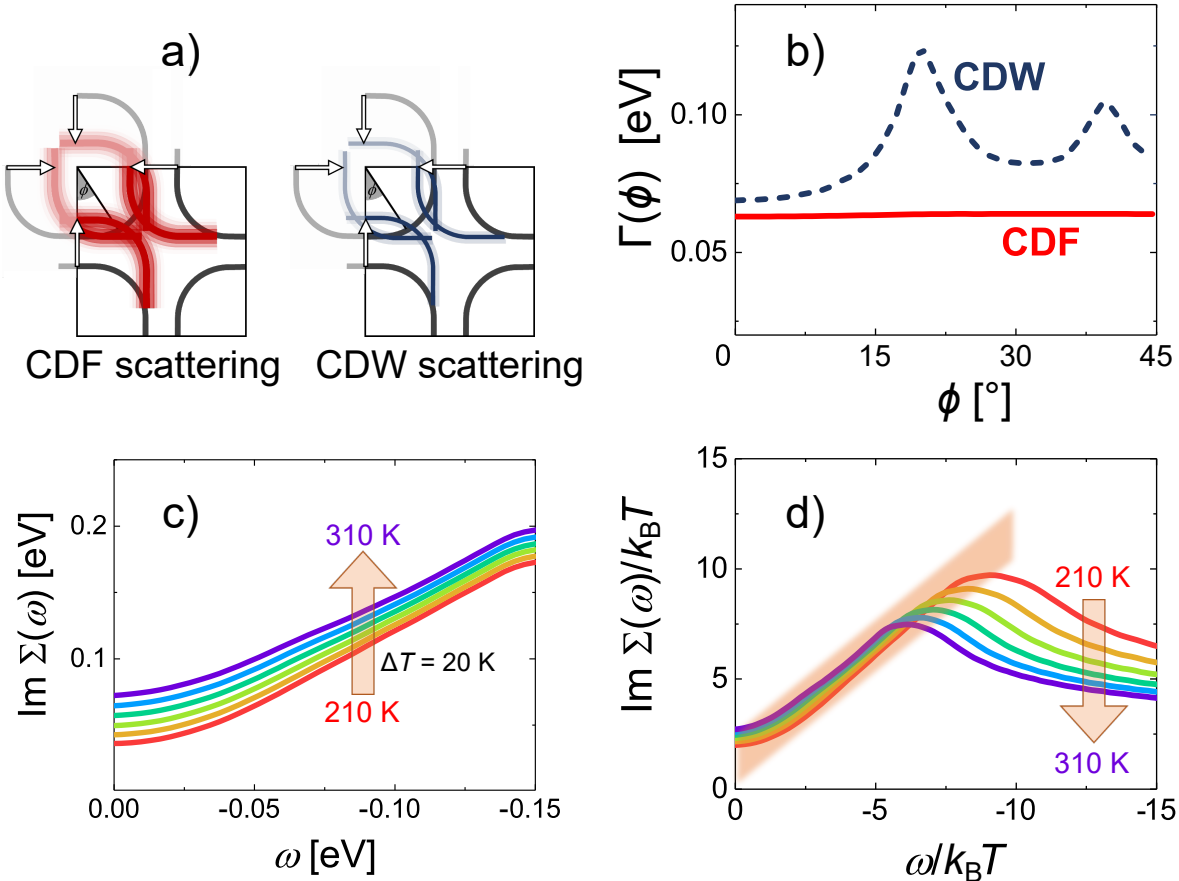


FIG. 2. (a) Sketch of the CDF and CDW mediated quasiparticle scattering. Owing to the broadness of CDFs in momentum space, all the Fermi surface (thick black line) can be scattered by low-energy CDFs over other portions of the Fermi surface, and no particular nesting condition is needed. The involvement of only the upper left branch of the Fermi surface in the Brillouin zone is displayed for clarity: The scattered portions of the Fermi surface (broad reddish areas) essentially cover the whole branch. Therefore the whole Fermi surface is affected in a nearly isotropic way. On the contrary, the CDWs are peaked in momentum space and scatter the Fermi surface states in rather restricted regions of other Fermi surface branches (hot spots). These occur where the bluish lines cross the thick black line. (b) Scattering rate [i.e., the imaginary part of the self-energy at zero frequency  $\Gamma(\phi) = \text{Im } \Sigma(\phi, T, \omega = 0)$ ] at a given temperature  $T$  as a function of the position on the Fermi surface, as identified by the angle  $\phi$  defined in panel (a). The nearly isotropic red line is due to the CDFs scattering only, while the blue dashed line includes the effects of scattering with CDWs. (c) Imaginary part of the electron self-energy as a function of the (negative) electron binding energy, at different temperatures above  $T_{\text{CDW}}$ , below which the CDW emerge to produce the narrow peak in RXS. The coupling between fermion quasiparticles and CDFs is  $g = 0.188 \text{ meV}$ . (d) Same as (c), but with both frequency and self-energy axes rescaled by the temperature ( $k_B$  is the Boltzmann constant), to highlight the approximate scaling behaviour at low frequency

spectrum. In many-body theory, this effect is customarily described by the electron self-energy, as reported in the diagram of Fig. 9 of the Supplementary Information (SI). In particular, the imaginary part of the electron self-energy,  $\text{Im } \Sigma$ , provides the broadening of the electron dispersion as measured, e.g., in angle-resolved photoemission experiments. We adopt the following strategy: a) we extract from the experimental inelastic RXS spectra the information on the dynamics of the CDFs (see the SI); b) we borrow from photoemission experiments the electron dispersion in the form of a tight-binding band structure

[21] (see the SI); c) we calculate the electron self-energy resulting from the coupling between CDFs and the electron quasiparticles. The result of our calculation is reported in Fig. 2. Clearly,  $\text{Im } \Sigma$  has a linear frequency dependence up to 0.1–0.15 eV (comparable to the one reported in the photoemission experiments of Refs. 22 and 23). At low frequencies  $\text{Im } \Sigma$  saturates at a constant value that increases linearly with increasing  $T$ . This is precisely the behaviour expected from the MFL expression of Eq. 1. This self-energy is reported along a specific (1,1) direction, but it is crucial to recognize that it is

also highly isotropic in momentum space. Fig. 2(c) indeed reports the scattering rate (i.e., the imaginary part of the self-energy at zero frequency)  $\Gamma(\phi) \equiv \Gamma_0 + \Gamma_\Sigma(\phi)$ . An isotropic scattering rate  $\Gamma_0$  representing the effect of quenched impurities has also been included. Our results, not only share with the data of Ref. 22 a similar form, but also display a scaling behavior, as reported in Fig. 2(d). As mentioned in Ref. 1, the isotropic linear-in-frequency self-energy behaviour, stemming from CDFs, is sufficient to produce a MFL behaviour in physical quantities like optical conductivity and Raman scattering.

The question then arises about the effects of the additional scattering induced by CDWs responsible for the well-known narrow peak (NP) observed by RXS [12] at temperatures below  $T_{CDW} \approx 150 - 200$  K. This additional scattering is anisotropic and confined in a small region of momentum space, as shown by the dashed blue curve of Fig. 2(b), possibly leading to a departure from the MFL behaviour below temperatures comparable with  $T^*$ .

### CDFs produce linear resistivity

Once the dynamics of the CDFs is identified by exploiting RXS experiments, one can investigate their effects on transport properties. The calculation of the electron resistivity is carried out within a standard Boltzmann-equation approach along the lines of Ref. 24 (for details see the SI). From the electron self-energy we obtain the zero frequency quasiparticle scattering rate along the Fermi surface  $\Gamma(\phi)$  defined above, and we use  $\Gamma_0$  as a fitting parameter, obtaining values ( $\approx 30 - 60$  meV) that are reasonable for impurity scattering. We also use the anisotropic Fermi wavevector along the Fermi surface, as obtained from the same band structure in tight-binding approximation [21] used for the self-energy calculation.

Fig. 3(a) displays the  $\rho(T)$  curve of the optimally doped NBCO film ( $T_c = 90$  K), studied in Ref. 2 (yellow curve). At high temperatures, the famous linear-in- $T$  behaviour of the resistivity is found and the data are quantitatively matched. This behaviour stems from the very isotropic scattering rate produced by the CDFs [red solid line in Fig. 2(b)], which, for this sample and in this temperature range, are the only observed charge excitations. At lower temperatures, below  $T^*$ , a discrepancy emerges between the theoretical expectation and the experimental evidence, since the expected saturation, due to the onset of a Fermi-liquid regime and to (isotropic) impurity scattering  $\Gamma_0$ , is experimentally replaced by a downturn of the resistivity. Such discrepancy occurs gradually in  $T$  when entering the pseudogap state, where other intertwined incipient orders set in (CDWs, Cooper pairing, etc.). These effects, which are outside our present scope, obviously lead to deviations from our theory, which only considers here the effects of CDFs (for the effects of CDWs see the SI). On the other hand, in the overdoped YBCO sample ( $T_c = 83$  K), the pseudogap and the intertwined orders are absent, while the broad peak related to CDFs is still present even at the lowest temperatures (see, Fig. S9 in Ref. 2). Here, our theoreti-

cal resistivity, related to the scattering rate produced by the CDFs, matches very well the experimental data, in the whole range from room temperature almost down to  $T_c$  [see Fig. 3(b)]. In particular, the agreement is rather good even at the lowest temperatures above  $T_c$ , where the upwards saturation due to onset of a Fermi-liquid regime is visible in the experimental curve too.

### Discussion and conclusions

The MFL behaviour has often been associated with some form of criticality, because it requires some low-energy scattering mechanism that could be provided by quantum-critical collective modes scattering in nearly the same way all the quasiparticles at the Fermi surface. However, the situation is usually more involved. Namely the quasicritical CDWs, observed below  $T_{CDW}$ , cannot be responsible for the MFL behaviour that persists up to the highest temperatures (for instance, the linear resistivity in LSCO or Bi2201 persists up to several hundreds of K). Moreover, they mediate anisotropic scattering, as it is usual for mediators with a finite modulation vector, leading to hot spots on the Fermi surface, which is not apt to produce the MFL behaviour [25]. This is instead obtained from CDFs with shorter correlation length, and low characteristic energy  $\omega_0$  of the order of 15 meV, which stays smaller than the temperature down to the lowest  $T \geq T_c$ , producing the linear resistivity. In some sense, although CDFs are rather overdamped, quite different from propagating phonons, the situation is similar to the linear resistivity due to phonons when the temperature is larger than the Debye temperature. The question is then, why CDFs have such a low characteristic energy. Although a full answer would require a microscopic theory, that is outside the scope of the present work, we see a relation to the proximity to the CDW quantum critical point. This nearby criticality brings at low energy all the charge collective fluctuations [26] (remember that CDFs and CDWs have similar characteristic wave vectors, indicating a close relationship), and even those which are prevented from becoming long-ranged (i.e., the CDFs) acquire a low characteristic energy.

The occurrence of CDW-mediated scattering below  $T_{CDW}$  opens an additional scattering channel that spoils the linear resistivity. However, our calculations give rise to an upturn of  $\rho(T)$  below  $T^*$ , at odds with the experimental evidence. In this case, we may conjecture that CDWs induce Cooper pairing [27] and the consequent paraconductivity fluctuations [28], together with the CDW-induced opening of pseudogap, may be responsible for the observed downturn of  $\rho(T)$  below  $T^*$ . To support this conjecture we may observe that, in the range of doping where CDWs are present, a crossover from the MFL linear to a purely quadratic resistive behavior appears in the pseudogapped state [3, 29]. In particular, above  $p = 1/8$ , the upper and lower bounds in temperature for such dependence have been associated to the onsets respectively of the CDW-related electronic nematicity [30] and of the superconducting fluctuations [31].

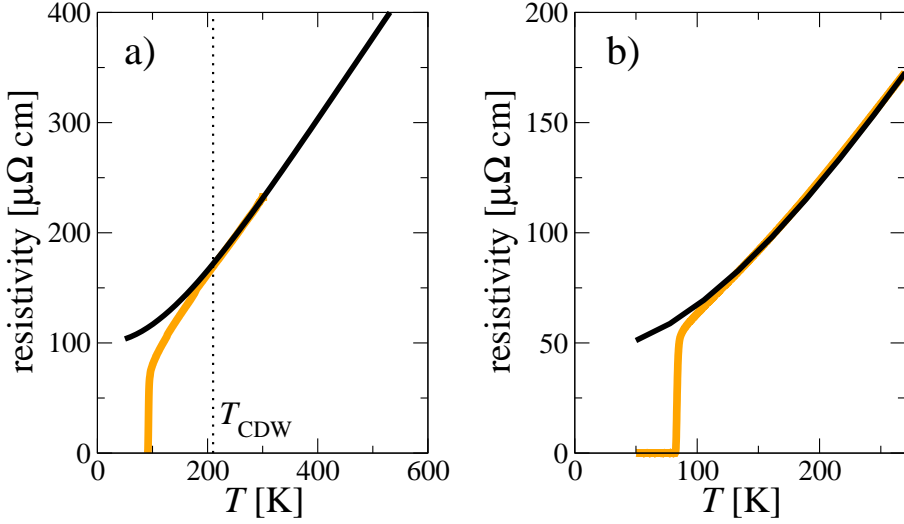


FIG. 3. (a) Experimental resistivity for an optimally doped ( $T_c = 93$  K) NBCO sample (yellow thick curve) compared to the theoretical result as obtained from the CDFs only (black solid line). The scattering rate includes an elastic scattering  $\Gamma_0$  due to quenched impurities,  $\Gamma(\phi) = \Gamma_0 + \text{Im } \Sigma(\phi, T, \omega = 0)$ . Here,  $\Gamma_0 = 62$  meV, and the coupling  $g = 0.188$  eV between quasiparticles and CDFs is the same as for the self-energy of Fig. 2. (b) Same as (a) for an overdoped YBCO sample ( $T_c = 83$  K). Here,  $\Gamma_0 = 28.5$  meV,  $g = 0.210$  eV.

Such occurrence hints at a possible role/intertwining of CDWs and Cooper pair fluctuations, which might be relevant to explain the transport below  $T^*$ .

We purposely avoided any assumption on the origin of CDFs: Once the dynamics of the CDFs is extracted from RXS experiments, we can well explain, *with the same parameter set*, both the MFL behaviour of the electron self-energy (therefore all the related anomalous spectral properties observed, e.g., in optical conductivity and Raman spectroscopy) and the famous linear-in- $T$  resistivity in the metallic state of high-temperature superconducting cuprates. We believe that our results provide a very sound step forward in the long-sought understanding of the important problem of the violation of the normal Fermi-liquid behaviour in cuprates.

**Acknowledgments** We thank C. Castellani, S. Kivelson, M. Le Tacon, M. Moretti Sala and T.P. Devreux for stimulating discussions. We acknowledge financial support from “University Research Project” of the ‘Sapienza’ University n. RM11715C642E8370 and by ERC-P-ReXS project (2016-0790) of the Fondazione CARIPLO and Regione Lombardia, in Italy. R. A. is supported by the Swedish Research Council (VR) under the project “Evolution of nanoscale charge order in super-

conducting YBCO nanostructures”. G.S. acknowledges support from the Deutsche Forschungsgemeinschaft.

### Appendix: Methodological details

In this Appendix, we illustrate the main steps of our procedure to extract information about CDWs and CDFs from the experimental RXS data. Further details can be found in the SI.

The CDW and CDF contributions to the RXS spectra are captured by a density response-function diagram as reported in Fig. 4 of the SI. In this framework we carry out a twofold task: on the one hand we show that dynamical CDFs and nearly critical CDWs account both for the RXS high-resolution, frequency dependent, spectra, and for the quasi-elastic momentum-dependent spectra. On the other hand, from the fitting of these experimental quantities, we extract the dynamical structure of these excitations needed to calculate the physical quantities discussed above.

According to this scheme, the CDW or CDF contribution to the low-energy RXS spectra is

$$I(\mathbf{q}, \omega) = A \text{Im } D(\mathbf{q}, \omega) b(\omega) \quad (2)$$

where  $b(\omega) \equiv [e^{\omega/T} - 1]^{-1}$  is the Bose distribution ruling the thermal excitation of CDFs and CDWs, and  $A$  is

a constant effectively representing the intricate photon-conduction electron scattering processes [32]. In Eq. (2),  $\text{Im } D(\mathbf{q}, \omega)$  is the imaginary (i.e., absorptive) part of the dynamical density-density correlator, which can describe either CDWs or CDFs. For both we adopt the standard Ginzburg-Landau form of the dynamical density-density correlator, typical of overdamped quantum critical Gaussian fluctuations [7, 8, 26],

$$D(\mathbf{q}, \omega) \equiv \left[ \omega_0 + \nu(\mathbf{q}) - i\omega - \frac{\omega^2}{\bar{\Omega}} \right]^{-1}, \quad (3)$$

where  $\omega_0 = \bar{\nu} \xi^{-2}$  is the characteristic energy of the fluctuations,  $\nu(\mathbf{q}) \approx \bar{\nu} |\mathbf{q} - \mathbf{Q}_c|^2$ ,  $\bar{\nu}$  determines the dispersion of the density fluctuations,  $\mathbf{Q}_c \approx (0.3, 0), (0, 0.3)$  is the characteristic critical wavevector (we work with dimensionless wavevectors, measured in reciprocal lattice units, r.l.u.) and  $\bar{\Omega}$  is a frequency cutoff. The sharper CDWs have a nearly critical character, with a marked temperature dependence of the square correlation length,  $\xi_{NP}^2(T)$ . In particular, if these fluctuations had a standard quantum critical character around optimal doping [7, 8, 26, 35], one would expect  $\xi_{NP}^2(T) \sim 1/T$ . The CDFs have a similar  $\mathbf{Q}_c$ , the main difference being in the behaviour of the correlation length, that, according to RXS experiments, increases significantly with decreasing the temperature and reaches up to 8-10 lattice spacings for the nearly critical CDWs, while the CDFs have correlation length in the range 2-3 lattice spacings, independently of the temperature.

Although high-resolution spectra provide a wealth of information, they are experimentally very demanding, so that RXS data are more often available in the form of quasi-elastic spectra corresponding to the frequency integration of the inelastic spectra, Eq. (2),

$$I(\mathbf{q}) = \int_{-\infty}^{+\infty} \frac{A \omega}{\left( \omega_0 + \nu(\mathbf{q}) - \frac{\omega^2}{\bar{\Omega}} \right)^2 + \omega^2} b(\omega) d\omega \quad (4)$$

$$\approx AT \text{Re } D(\mathbf{q}, \omega = 0) = \frac{AT}{\bar{\nu} |\mathbf{q} - \mathbf{Q}_c|^2 + \omega_0}. \quad (5)$$

The approximate equality holds provided  $T$  is large enough so that  $b(\omega) \approx T/\omega$  in the frequency range selected by the density-density correlation function. Although we checked that the parameters extracted from the fits of the experimental spectra comply with this assumption, we always fitted experiments with the exact expression (4). Our first goal is to extract from the experiments all the parameters entering the CDW and CDF correlators,  $\omega_0, \bar{\nu}, \mathbf{Q}_c$  and  $\bar{\Omega}$ .

Since high-resolution and quasi-elastic spectra provide different complementary information, we adopted a bootstrap strategy in which we first estimated the dynamical scale  $\omega_0$  from high-resolution at the largest temperatures, where the narrow peak due to CDWs is absent and all collective charge excitations are CDFs. Then we used this information to fit the quasi-elastic peaks to extract the relative weight (intensity) of the narrow and broad

contributions. Once this information is obtained, we go back to high resolution spectra at all temperature since we now know the relative weight of the CDF and CDW contribution at all temperatures.

More specifically, the quasi-elastic peak has a composite character and, once the (essentially linear) background measured along the (1, 1) direction is subtracted (see, e.g., Fig. 2 A-D in Ref. 2), the peak may be decomposed into two approximately Lorentzian curves, corresponding to a narrow, strongly temperature dependent peak due to the standard nearly critical CDWs arising below  $T \sim 200$  K and to a broad peak due to the CDFs with a temperature dependence only stemming from the thermal excitation encoded in the Bose distribution. This is the main outcome of the RIXS experiments reported in Ref. 2. We thus fitted each of the two peaks with equation (5). From the fits, one can extract the overall intensity parameter  $A$  and the ratio  $\omega_0/\bar{\nu} = \xi^{-2}$ . Since only this ratio determines the width of the quasi-elastic spectra, we need a separate measure to disentangle  $\omega_0$  and  $\bar{\nu}$ , so we used the high-resolution information on  $\omega_0$  for the broad peaks (BP) at  $T = 150$  K and  $T = 250$  K to extract  $\bar{\nu}_{BP} \approx 1400$  meV at these temperatures. The same procedure cannot be adopted for the narrow CDW peaks, which always appear on top of (and are hardly unambiguously separated from) the broad CDF contribution. Nevertheless, to obtain a rough estimate, we investigated the high-resolution spectra at low temperature (see the SI), where the maximum intensity should mostly involve the narrow peak to extract the characteristic energy of the quasi-critical CDWs obtaining, as expected, much lower values  $\omega_0^{NP} \approx 1-3$  meV (although these low values are less reliable, due to the relatively low resolution of the frequency-dependent spectra). These estimates allow to extract values of  $\bar{\nu}_{NP} \approx 800$  meV for the CDWs, comparable with those of the CDFs, suggesting a common electronic origin of the two types of charge fluctuations. To reduce the fitting parameters to a minimum, although subleading temperature dependencies of the high-energy parameters  $\bar{\nu}$  and  $\bar{\Omega}$  over a broad temperature range can be expected, we kept those parameters constant. We also assumed a constant  $\omega_0$  for the CDFs, to highlight the non-critical nature of these fluctuations.

## SUPPLEMENTARY INFORMATION

### I. EXTRACTING THE CDF AND CDW DYNAMICS FROM RIXS SPECTRA

#### A. The fitting strategy

As mentioned in the Appendix, the CDW or CDF contribution to the low-energy RIXS spectra is

$$I(\mathbf{q}, \omega) = A \operatorname{Im} D(\mathbf{q}, \omega) b(\omega), \quad (6)$$

where  $b(\omega) \equiv [e^{\omega/T} - 1]^{-1}$  is the Bose distribution of charge fluctuations and  $A$  is a constant effectively representing the intricate photon-conduction electron scattering processes [32], while  $\operatorname{Im} D(\mathbf{q}, \omega)$  is the imaginary part of the dynamical density-density correlator describing either CDWs or CDFs. This contribution to RIXS spectra corresponds to the Feynman diagram of Fig. 4(a). At  $\mathbf{q} = \mathbf{Q}_c$  high-resolution RIXS spectra have the form reported in Fig. 4(b). Once the

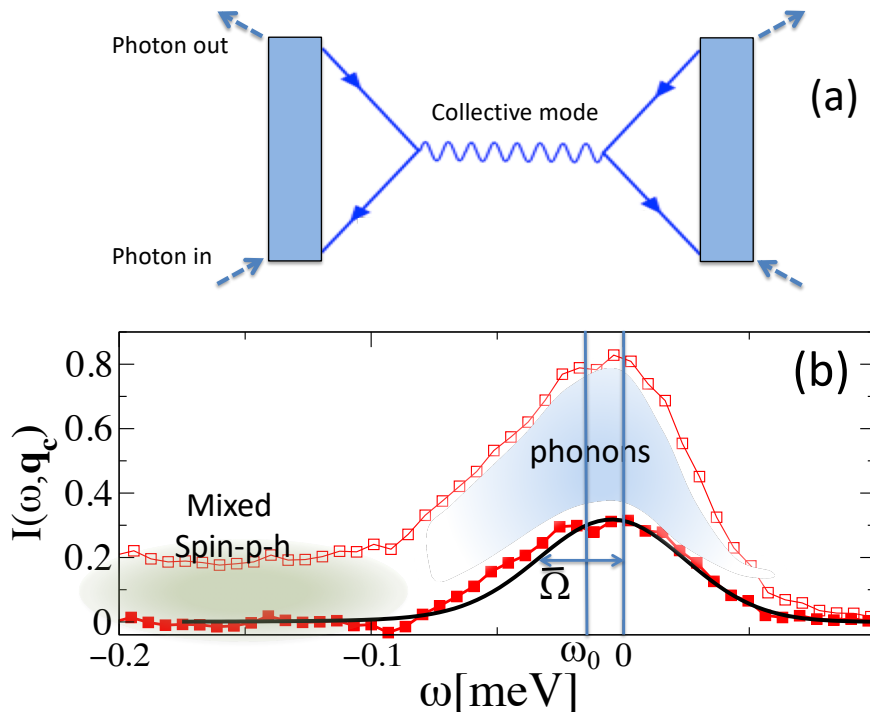


FIG. 4. (a) Feynman diagram schematising the contribution of a charge collective mode (wavy line) to the RIXS spectra. The shaded rectangles represent the coupling between the incoming and outgoing photons (dashed blue lines) with the conduction electrons (solid blue lines). (b) Example of an high-resolution RIXS spectrum of an optimally doped ( $T_c = 90$  K)  $\text{Nd}_{1+x}\text{Ba}_{2-x}\text{Cu}_3\text{O}_{7-\delta}$  sample at  $T = 250$  K and at the critical wavevector for CDFs  $\mathbf{q} = \mathbf{Q}_c \approx (0.3, 0)$  r.l.u. (empty squares). The contribution of phononic excitations and of the spin and particle-hole excitations are shaded in light blue and green, respectively. The “pure” CDFs spectrum obtained subtracting these contributions is reported with solid squares.

spin and phonon contributions are subtracted, valuable information can be extracted to determine the dynamics of the CDFs and CDWs. Specifically, using Eq. (6), one can fit the high-resolution spectra at high temperature (where CDWs are not present) to find the dynamical scale  $\omega_0$  of CDFs. Then this information can be used to fit the quasi-elastic peaks and extract the relative weight (intensity) of the narrow and broad contributions at all temperatures. Once this information is obtained, the relative weight of the CDF and CDW contribution at all temperatures is known, and one can go back to high-resolution spectra at lower  $T$ .

The peak in the quasi-elastic RIXS spectra has a composite character and, once the background measured along the (1, 1) direction is subtracted (see, e.g., Fig. 2 A-D in Ref. 2), the peak may be decomposed into two approximately Lorentzian contributions. The narrow peak, a strongly temperature dependent peak, is due to the well-known nearly critical CDWs arising below  $T_{CDW} \approx 200$  K (for the sample at optimal doping), while a broad peak is also present due to the CDFs, which decreases by lowering  $T$ , because of the thermal excitation encoded in the Bose distribution

[see also Eq. (5) in the Appendix]. The identification of this broad peak is the main outcome of the RIXS experiments reported in Ref. 2. We fitted the experimental data (blue points in Fig. 5) with Eq. (4) of the main text. Hereafter, the labels *NP* and *BP* are used to mark the quantities that refer to the narrow and broad peak, respectively.

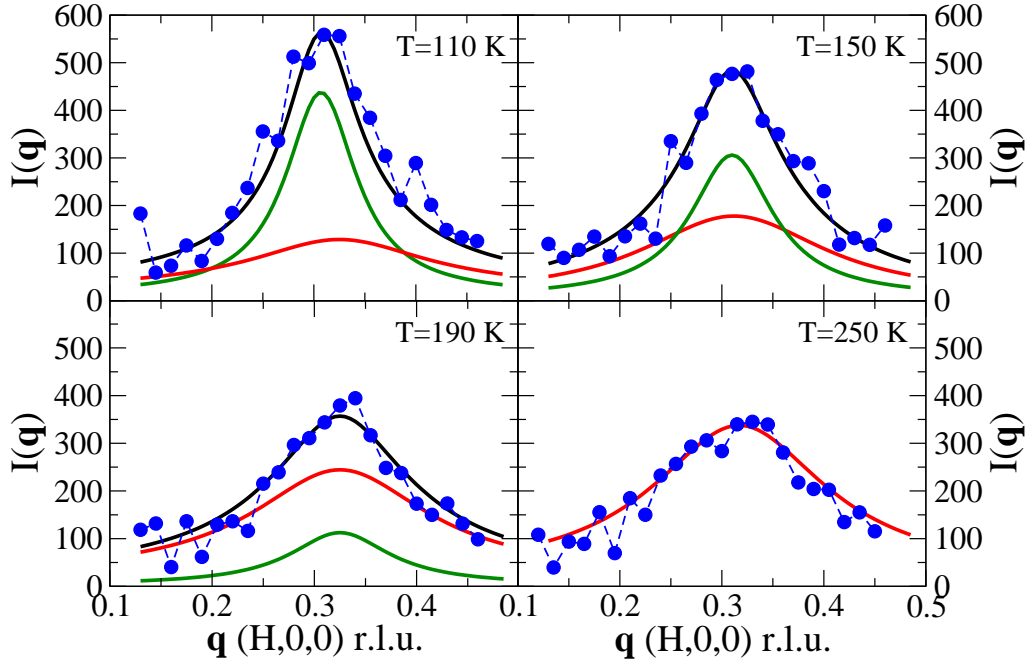


FIG. 5. Quasi-elastic RIXS spectra along the (H,0) direction of an optimally doped ( $T_c = 90$  K)  $\text{Nd}_{1+x}\text{Ba}_{2-x}\text{Cu}_3\text{O}_{7-\delta}$  sample (blue dots), at four different temperatures above  $T_c$ . The subtraction of the linear background measured along the (1,1) direction has been performed. The fitting curve (black solid line) is the sum of two contributions: a narrow peak (attributed to nearly critical CDWs, green solid lines) and a broad peak due to CDFs (red solid line).

From the fits one can extract the overall intensity parameter  $A$  and the ratio  $\omega_0/\bar{\nu}$ . Since only this ratio determines the width of the quasi-elastic spectra, we need a separate measure to disentangle  $\omega_0$  and  $\bar{\nu}$ . Therefore for the optimally doped sample with  $T_c = 90$  K we used the high-resolution information on  $\omega_0$  for the broad peaks at  $T = 250$  K to extract  $\bar{\nu}_{BP} \approx 1400$  meV at these temperatures. The same procedure cannot be adopted for the narrow CDW peaks, which always appear on top of (and are hardly unambiguously separated from) the broad CDF contribution. Nevertheless, to obtain a rough estimate, we investigated the high-resolution spectra at low temperature, where the maximum intensity should mostly involve the narrow peak to extract the characteristic energy of the quasi-critical CDWs obtaining, as expected, much lower values  $\omega_0^{NP} \approx 1 - 3$  meV (although these low values are less reliable, due to the relatively low resolution of the frequency-dependent spectra).

These estimates allow to extract values of  $\bar{\nu}_{NP} \approx 800$  meV for the CDWs in qualitative agreement with those of the CDFs. This suggests that common electronic degrees of freedom (e.g., the Fermion quasiparticles in the approach of Refs. [7, 8, 35]) underlie both kinds of charge density excitations. To reduce the fitting parameters to a minimum, although subleading temperature dependencies of the high-energy parameters  $\bar{\nu}$  and  $\bar{\Omega}$  over a broad temperature range can be expected, we kept those parameters constant. We also assumed a constant  $\omega_0$  for the CDFs, to highlight the non-critical nature of these fluctuations.

This fitting procedure also allows to identify the relative intensity of the narrow and broad peaks, which is reported in the inset of Fig. 6, where it is clear that the narrow peak arises below  $T_{CDW} \approx 200$  K and grows at the expense of the broad peak.

Once the fitting of the quasi-elastic spectra was carried out, we analysed the high-resolution RIXS spectra at lower temperatures. At this stage, but for a common overall factor (the overall intensity of high-resolution spectra being unrelated to the intensity of the low-resolution spectra, due to the different time and conditions of the corresponding measures) we have no more free parameters to use because the characteristic energies and the relative weight of

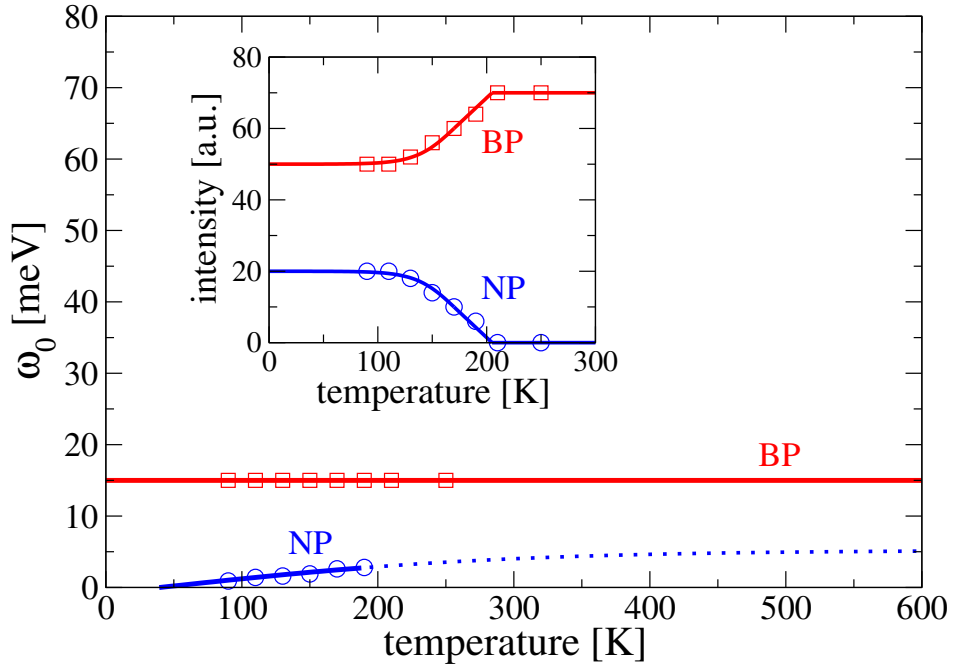


FIG. 6. The fit parameters from Tab. I and the corresponding fitting functions Eqs. (7)–(10) which are used to calculate the resistivity as a function of temperature.

the CDWs and CDFs were determined. Subtracting the phonon and spin/particle-hole excitations (as determined from the high-resolution spectra at  $\mathbf{q} \parallel (1, 1)$ ), one obtains spectra where the contribution of CDFs and CDWs is only (or predominantly) present. Then we obtained spectra and the fits of Fig. 7. These spectra are taken at three representative temperatures: at high temperature ( $T = 250$  K), where only CDFs are present, at intermediate temperature ( $T = 150$  K), where CDFs and CDWs coexist, and at low temperature ( $T = T_c = 90$  K), where the CDWs are more pronounced than CDFs (see also Fig. 5).

### B. The parameters of the CDW and CDF dynamics

Tab. I reports the temperature dependence of the parameters which determine the CDW and CDF correlators and which have been determined within the procedure discussed above and in the Appendix.

$T$ [K]	$\omega_0^{BP}$ [meV]	$Q_c^{BP}$ [r.l.u.]	$A_{BP}$	$\nu_{BP}$ [meV]	$\omega_0^{NP}$ [meV]	$Q_c^{NP}$ [r.l.u.]	$A_{NP}$	$\nu_{NP}$ [meV]	$\bar{\Omega}_{NP,BP}$ [meV]
90	15	0.312	50	1400	0.9	0.310	20	800	30
110	15	0.325	50	1400	1.4	0.307	20	800	30
130	15	0.316	52	1400	1.6	0.307	18	800	30
150	15	0.312	56	1400	1.9	0.31	14	800	30
170	15	0.325	60	1400	2.6	0.325	10	800	30
190	15	0.325	64	1400	2.8	0.325	6	800	30
210	15	0.310	70	1400					30
250	15	0.317	70	1400					30
62	10	0.275	100	2000					30

TABLE I. Temperature dependence of the fitting parameters as discussed in the text. Above the double line the parameters refer to the optimally doped sample with  $T_c = 90$  K, while below the double line we report the parameters of the overdoped sample with  $T_c = 83$  K.

For the computation of the temperature dependence scattering function and resistivity the temperature dependent

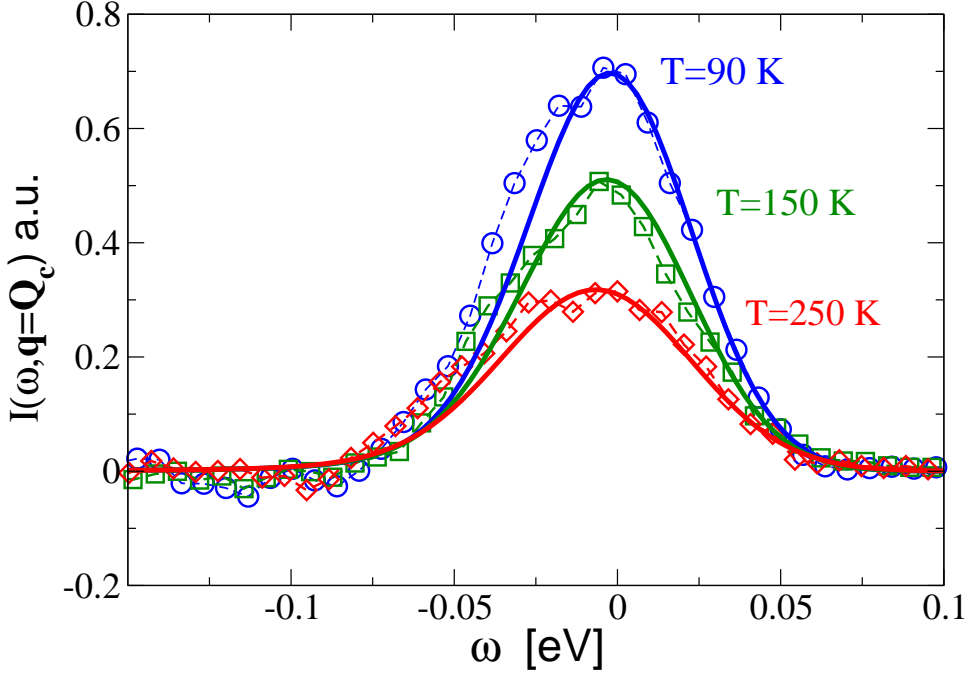


FIG. 7. High-resolution RIXS spectra of an optimally doped ( $T_c = 90$  K)  $\text{Nd}_{1+x}\text{Ba}_{2-x}\text{Cu}_3\text{O}_{7-\delta}$  sample. The fitting parameters are taken from Tab. I and only a factor common to all theoretical curves for the overall intensity has been adjusted. The horizontal axis of the experimental data has been slightly shifted (but within the estimated  $\pm 4$  meV energy error bar) to match the right part of the experimental and theoretical spectra in the region where the Bose distribution factor cuts the positive excitation energies:  $-2$  meV for the  $T = 90$  K data,  $+4$  meV for the  $T = 150$  K data, and  $-2$  meV for the  $T = 250$  K data.

mass and intensity parameters of Tab. I have been fitted by the following functions

$$\omega_0^{NP} = 5.2 \tanh \frac{T - 39.8 \text{ K}}{254.3 \text{ K}} \text{ meV} \quad (7)$$

$$\omega_0^{BP} = 15 \text{ meV} \quad (8)$$

$$A_{BP} = \begin{cases} 50 + 10 \left[ 1 + \tanh \frac{T - 170 \text{ K}}{35 \text{ K}} \right] & \text{for } T < 170 \text{ K} \\ 60 + 0.286 (T - 170 \text{ K}) & \text{for } 170 \text{ K} < T < 205 \text{ K} \\ 70 & \text{for } T > 205 \text{ K}, \end{cases} \quad (9)$$

$$A_{NP} = \begin{cases} 10 \left[ 1 - \tanh \frac{T - 170 \text{ K}}{35 \text{ K}} \right] & \text{for } T < 170 \text{ K} \\ 10 - 0.286 (T - 170 \text{ K}) & \text{for } 170 \text{ K} < T < 205 \text{ K} \\ 0 & \text{for } T > 205 \text{ K}, \end{cases} \quad (10)$$

which are shown in Fig. 6 together with the parameters from Tab. I.

## II. CALCULATION OF THE RESISTIVITY

We evaluate the in-plane resistivity following the approach derived in Ref. 24. We obtain

$$\frac{1}{\rho} = \frac{e^2}{\pi^3 \hbar} \frac{2\pi}{d} \int d\phi \frac{k_F(\phi) v_F(\phi) \cos^2(\phi - \gamma)}{\Gamma(\phi) \cos(\gamma)}, \quad (11)$$

where  $k_F(\phi)$ ,  $v_F(\phi)$ , and  $\Gamma(\phi)$  denote the angular dependence of the Fermi momentum, Fermi velocity, and scattering rate along the Fermi surface (see inset of Fig. 8), and

$$\gamma = \text{atan} \left( \frac{1}{k_F} \frac{\partial k_F}{\partial \phi} \right).$$

The scattering rate  $\Gamma(\phi) \equiv \Gamma_0 + \Gamma_\Sigma(\phi)$  includes an elastic scattering rate  $\Gamma_0$ , and the scattering rate due to CDWs or CDFs,  $\Gamma_\Sigma(\phi) \equiv \text{Im} \Sigma(k_F(\phi), \omega = 0)$ , where  $\Sigma(\mathbf{k}, \omega)$  is the electron self-energy (see below, Sec. III B).

The electron dispersion  $\varepsilon_k$  includes nearest-, next-nearest- and next-next-nearest-neighbor hopping terms generic for cuprates [21]. The in-plane lattice constant for YBCO is taken as  $a = 3.85 \text{ \AA}$  and the  $c$ -axis lattice constant is  $d = 11.7 \text{ \AA}$ . The bilayer structure of YBCO is effectively taken into account by multiplying Eq. (11) by a further factor of 2.

The imaginary part of the electron self-energy is [36]

$$\text{Im} \Sigma(\mathbf{k}, \omega) = g^2 \int \frac{d^2 \mathbf{q}}{(2\pi)^2} \frac{(\omega - \varepsilon_{\mathbf{k}-\mathbf{q}})[b(\varepsilon_{\mathbf{k}-\mathbf{q}}) + f(\varepsilon_{\mathbf{k}-\mathbf{q}} - \omega)]}{[\omega_0 + \bar{\nu} \eta_{\mathbf{q}} - (\omega - \varepsilon_{\mathbf{k}-\mathbf{q}})^2/\Omega]^2 + (\omega - \varepsilon_{\mathbf{k}-\mathbf{q}})^2}, \quad (12)$$

where  $b(z) = [e^{z/T} - 1]^{-1}$  is the Bose function,  $f(z) = [e^{z/T} + 1]^{-1}$  is the Fermi function,  $g$  is the coupling between electrons and CDFs or CDWs, and  $(2\pi)^2 \eta_q = 4 - 2\cos(q_x - Q_x^c) - 2\cos(q_y - Q_y^c)$  contains the information about the CDW/CDF vector  $\mathbf{Q}_c$ . The function  $\eta_q$  is scaled by  $1/(2\pi)^2$  because in the fit to RIXS the wavevector is defined in r.l.u. (see Sec. I.A). For the evaluation of  $\Gamma_\Sigma$  we sum over all 4 equivalent wavevectors  $(\pm Q_c, 0)$  and  $(0, \pm Q_c)$  with  $Q_c \approx 0.3 \text{ r.l.u.}$

### III. EFFECTIVE MEDIUM THEORY

#### A. Resistivity

As discussed above, in the main text, the RIXS spectra have a composite nature showing that CDFs and CDWs are both present in the system below a crossover temperature  $T_{CDW}$ . The question naturally arises about the origin of the two peaks. The first possibility is that they arise from a single fluctuating mode, which is uniformly present in the system, having a complex dynamical structure to reproduce the composite two-peak structure. The alternative is that CDFs and CDWs simply occur in spatially separated regions. In this second case the composite character of the spectra would be related to an inhomogeneous character of the systems: charge fluctuations would occur over the whole system at low energy as a natural generic tendency to CDW quantum criticality, but only in a smaller portion of the  $CuO_2$  planes they would find the favourable conditions (electron density, disorder, strain, ...) to fully realise this criticality allowing the growth of correlations at longer and longer distances, i.e., smaller and smaller characteristic energy. These regions would then give rise to the nearly critical CDWs responsible for the temperature dependent narrow peak. However, over most of the sample, criticality would remain latent in the form of dynamical (very) short-ranged CDFs. While for the first case it is not easy to identify a generic robust mechanism, it is much simpler to describe a situation in which the broad and narrow peak may occur in different spatial regions (patches) of the sample. In this case, we compute the resulting resistivity within an effective medium approach [37]. In each patch the resistivity is derived from the scattering rate  $\Gamma(\phi)$  due to the specific charge fluctuation dominant in that patch, while, to reduce the number of parameters, we take the same elastic scattering and coupling to the self-energy for broad peak and narrow peak patches. Denote with  $\rho_{BP, NP}$  the resistivity of broad- and narrow-peak patches, respectively, and  $x_{BP, NP}$  are the corresponding concentrations. Then, the solution of the equation

$$\sum_{i=BP, NP} x_i \frac{\rho_i - \rho}{\rho_i + \rho} = 0 \quad (13)$$

yields

$$\rho = \frac{1}{2} \left\{ (\rho_{BP} - \rho_{NP})(x_{BP} - x_{NP}) + \sqrt{(\rho_{BP} - \rho_{NP})^2(x_{BP} - x_{NP})^2 + 4\rho_{BP}\rho_{NP}} \right\}. \quad (14)$$

The concentrations of narrow and broad peak patches are obtained from

$$x_{BP} = \frac{A_{BP}}{A_{BP} + A_{NP}},$$

$$x_{NP} = \frac{A_{NP}}{A_{BP} + A_{NP}},$$

where  $A_{BP, NP}$  are the intensities extracted from the fit of the RIXS data. While the main panel of Fig. 6 displays the temperature dependence of the CDF (red symbols and lines) and CDW (blue symbols and lines) energy scales  $\omega_0$ , the inset reports the fitted intensity of the broad and narrow peaks as extracted from the quasi-elastic RIXS spectra. Assuming that the coupling of the scattered photons with the collective modes is the same for CDFs and CDWs, the difference in the red and blue curves merely reflects the different volume fraction of the regions where CDFs (red) or CDWs (blue) are present.

Once the above parameters are determined and the scattering rates are found from the calculation of the electron self-energies (see below), the resistivity can finally be calculated. The results are displayed in Fig. 8.

A possible inhomogeneous scenario for magnetotransport in cuprates was recently proposed [11] and described within the effective medium theory, indicating that also magnetotransport experiments may provide evidence in favor of inhomogeneous landscapes in these systems. The effect of a magnetic field within our CDF/CDW scenario can be studied along the same lines [38].

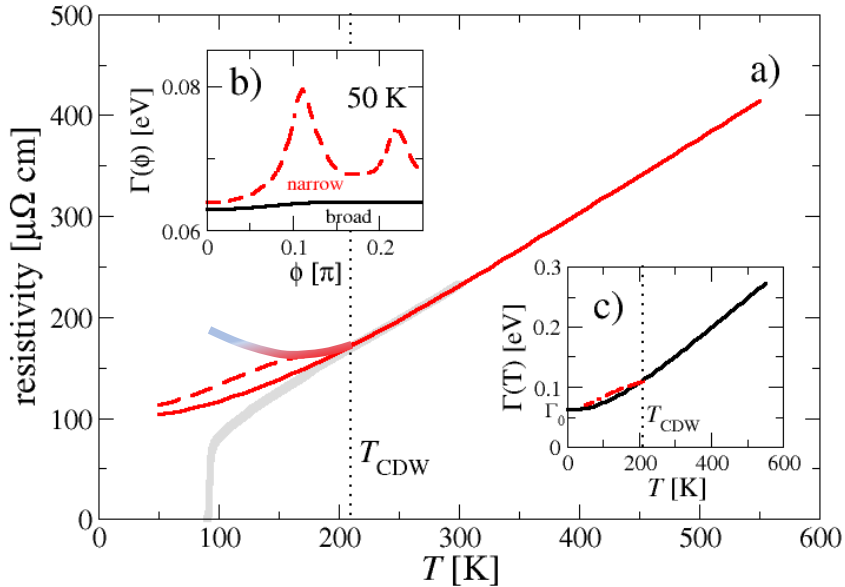


FIG. 8. Resistivity data and fit of an optimally doped ( $T_c = 90$  K)  $\text{Nd}_{1+x}\text{Ba}_{2-x}\text{Cu}_3\text{O}_{7-\delta}$  sample. The thick gray line is the experimental curve, while the red solid line is the result of theoretical calculations with the CDF contribution only (as in Fig. 3 of the main text). Below  $T_{CDW}$  the additional scattering due to CDWs generically produce an increase of the resistivity represented by the thick red-to-blue curve. Taking into account this additional scattering within the effective medium theory with the relative weights of CDFs and CDWs of Tab. I, the red dashed curve is obtained. The relative contributions of CDFs and CDWs to the scattering rate along the Fermi surface and (mediated on the Fermi surface) as a function of  $T$  are reported in the insets (b) and (c), respectively.

Of course our theoretical approach disregards the possible effects of CDWs in inducing pairing (hence triggering paraconductive fluctuations) and in modifying the quasiparticle spectrum leading to pseudogap opening and Fermi surface modifications, that could account for the downward bending of the experimental resistivity, which is missed by theoretical calculations.

## B. Self-energy

We define the Green functions in the narrow and broad peak regions as

$$G_{BP}(\mathbf{k}, \omega) = \frac{1}{\omega - \varepsilon_{\mathbf{k}} - \Sigma_{BP}(\mathbf{k}, \omega)} \quad (15)$$

$$G_{NP}(\mathbf{k}, \omega) = \frac{1}{\omega - \varepsilon_{\mathbf{k}} - \Sigma_{NP}(\mathbf{k}, \omega)}, \quad (16)$$

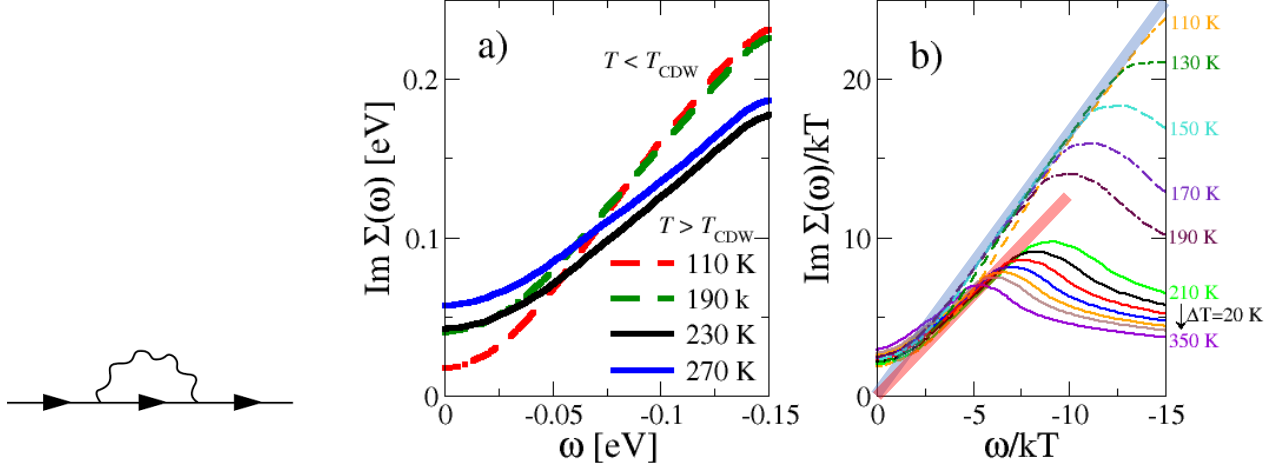


FIG. 9. Feynman diagram of the electron self-energy at the lowest perturbative order. The solid lines represent the electron propagator, while the wavy line represents either the CDF or the CDW correlator. (a) Electronic self-energy at  $T > T_{CDW}$  (black and blue solid lines) where only the CDFs contribute to the quasiparticle scattering. The dashed red and green lines report instead the self-energy for  $T < T_{CDW}$ , where also the anisotropic scattering due to CDWs is present. The coupling between fermion quasiparticles and CDFs (and CDW for  $T < T_{CDW}$ ) is  $g = 0.188$  meV. The momentum is on the Fermi surface along the diagonal (1,1) direction. (b) The rescaled self-energy has a characteristic collapse with a linear frequency dependence, but with a larger slope for  $T < T_{CDW}$  due to the additional CDW scattering.

where  $\varepsilon_{\mathbf{k}}$  is the electron dispersion in the form of a tight-binding band structure as obtained from photoemission experiments [21]. Of course the tight-binding parameters fitting the experimental dispersions already include the effect of the real part of the self-energy and therefore we use these values just as parameters representative of various cuprates in order to get the right order of magnitude of the energy scales in our single-band effective model.

We average Eqs. (15) and (16) to yield an effective Green function

$$G^{eff}(\mathbf{k}, \omega) = x_{NP} G_{NP}(\mathbf{k}, \omega) + x_{BP} G_{BP}(\mathbf{k}, \omega) \equiv \frac{1}{\omega - \varepsilon_{\mathbf{k}} - \Sigma^{eff}(\mathbf{k}, \omega)}, \quad (17)$$

with  $x_{NP} + x_{BP} = 1$ . The last identity in Eq. (17) defines the effective self-energy  $\Sigma^{eff}(\mathbf{k}, \omega)$ , which is then found by means of Eqs. (15,16), yielding

$$\Sigma^{eff}(\mathbf{k}, \omega) = \omega - \varepsilon_{\mathbf{k}} - \left[ \frac{x_{BP}}{\omega - \varepsilon_{\mathbf{k}} - \Sigma_{BP}(\mathbf{k}, \omega)} + \frac{x_{NP}}{\omega - \varepsilon_{\mathbf{k}} - \Sigma_{NP}(\mathbf{k}, \omega)} \right]^{-1} \quad (18)$$

The results are shown in Fig. 9.

It is clear that the self-energy has a characteristic MFL behaviour up to energies of order 0.1-0.15 eV, with a linear frequency dependence saturating at constant values at low frequency. These constant values increase with  $T$ , again according to the customary MFL behaviour. We notice, however, that, while the self-energy above  $T_{CDW}$ , due to the large width in momentum of the CDFs scatterers is nearly the same over the whole Fermi surface, the self-energy below  $T_{CDW}$  changes along the Fermi surface due to the anisotropic CDW scattering, thereby violating the canonical MFL behaviour.

[1] Varma, C. M., Littlewood, P. B., Schmitt-Rink, S., Abrahams, E., & Ruckenstein, A. E. Phenomenology of the Normal State of Cu-O High-Temperature Superconductors, *Phys. Rev. Lett.* **63**, 1996 (1989).

[2] Arpaia, R., Caprara, S., Fumagalli, R., De Vecchi, G., Peng, Y. Y., Andersson, E., Betto, D., De Luca, G. M., Brookes, N. B., Lombardi, F., Salluzzo, M., Braicovich, L., Di Castro, C., Grilli, M., & Ghiringhelli, G. Dynamical charge density fluctuations pervading the phase diagram of a Cu-based high- $T_c$  superconductor. arXiv:1809.04949.

[3] Arpaia, R., Andersson, E., Trabaldo, E., Bauch, T., & Lombardi, F. Probing the phase diagram of cuprates with  $\text{YBa}_2\text{Cu}_3\text{O}_{7-\delta}$  thin films and nanowires. *Phys. Rev. Materials* **2**, 024804 (2018).

[4] Aji, V. & Varma, C. M. Theory of the Quantum Critical Fluctuations in Cuprate Superconductors. *Phys. Rev. Lett.* **99**, 067003 (2007).

[5] Abanov, Ar., Chubukov, A. & Schmalian, J. Quantum-critical theory of the spin-fermion model and its application to cuprates: normal state analysis. *Adv. Phys.* **52**, 119 (2003), and references therein.

[6] Norman, M. R. & Chubukov, A. V. High-frequency behavior of the infrared conductivity of cuprates. *Phys. Rev. B* **73**, 140501R (2006).

[7] Castellani, C., Di Castro, C. & Grilli, M. Singular quasiparticle scattering in the proximity of charge instabilities. *Phys. Rev. Lett.* **75**, 4650 (1995).

[8] Castellani, C., Di Castro, C., & Grilli, M. Non-Fermi-liquid behavior and d-wave superconductivity near the charge-density-wave quantum critical point. *Z. Phys. B* **103**, 137 (1996).

[9] Kivelson, S. A., Bindloss, I. P., Fradkin, E., Oganesyan, V. , Tranquada, J. M., Kapitulnik, A., & Howald, C. How to detect fluctuating stripes in the high-temperature superconductors. *Rev. Mod. Phys.* **75**, 1201 (2003), and references therein.

[10] Caprara, S., Grilli, M., Di Castro, C., & Seibold, G. Pseudogap and (An)isotropic Scattering in the Fluctuating Charge-Density Wave Phase of Cuprates *J. Supercond. Nov. Magn.* **30**, 25-30 (2017).

[11] Patel, A. A., McGreevy, J., Arovas, D. P., & Sachdev S. Magnetotransport in a Model of a Disordered Strange Metal. *Phys. Rev. X* **8**, 021049 (2018).

[12] Ghiringhelli, G., et al. Long-Range Incommensurate Charge Fluctuations in  $(\text{Y},\text{Nd})\text{Ba}_2\text{Cu}_3\text{O}_{6+x}$ . *Science* **337**, 821-825 (2012).

[13] Achkar, A. J., et al. Distinct charge orders in the planes and chains of ortho-III-ordered  $\text{YBa}_2\text{Cu}_3\text{O}_{6+\delta}$  superconductors identified by resonant elastic x-ray scattering. *Phys. Rev. Lett.* **109**, 167001 (2012).

[14] Tabis, W., et al. Charge order and its connection with Fermi-liquid charge transport in a pristine high- $T_c$  cuprate. *Nat. Comm.* **5**, 5875 (2014).

[15] Comin, R., et al. Charge order driven by Fermi-arc instability in  $\text{Bi}_{2-x}\text{La}_x\text{CuO}_{6+\delta}$ . *Science* **343**, 390-392 (2014).

[16] Blanco-Canosa, S., et al. Resonant x-ray scattering study of charge-density wave correlations in  $\text{YBa}_2\text{Cu}_3\text{O}_{6+\delta}$ . *Phys. Rev. B* **90**, 054513 (2014).

[17] Keimer, B., Kivelson, S. A., Norman, M. R., Uchida, S., & Zaanen, J. From quantum matter to high-temperature superconductivity in copper oxides. *Nature* **518**, 179 (2015).

[18] Gerber, S., et al. Three-dimensional charge density wave order in  $\text{YBa}_2\text{Cu}_3\text{O}_{6.67}$  at high magnetic fields. *Science* **350**, 949-952 (2015).

[19] Comin, R. & Damascelli, A. Resonant x-ray scattering studies of charge order in cuprates. *Annu. Rev. Condens. Matter Phys.* **7**, 369-405 (2016).

[20] Peng, Y. Y., et al. Re-entrant charge order in overdoped  $(\text{Bi}, \text{Pb})_{2.12}\text{Sr}_{1.88}\text{CuO}_{6+\delta}$  outside the pseudogap regime. *Nat. Mater.* **17**, 697 (2018).

[21] Meevasana, W., et al. Hierarchy of multiple many-body interaction scales in high-temperature superconductors. *Phys. Rev. B* **75**, 174506 (2007).

[22] Valla, T., et al. Evidence for Quantum Critical Behavior in the Optimally Doped Cuprate  $\text{Bi}_2\text{Sr}_2\text{CaCu}_2\text{O}_{8+\delta}$ . *Science* **285**, 2110 (1999).

[23] Bok J. M., et al., Momentum dependence of the single-particle self-energy and fluctuation spectrum of slightly underdoped  $\text{Bi}_2\text{Sr}_2\text{CaCu}_2\text{O}_{8+\delta}$  from high-resolution laser angle-resolved photoemission. *Phys. Rev. B* **81**, 174516 (2010).

[24] Hussey, N. E. The normal state scattering rate in high- $T_c$  cuprates. *Eur. Phys. J. B* **31**, 495 (2003).

[25] Hlubina, R. & Rice, T. M. Resistivity as a function of temperature for models with hot spots on the Fermi surface *Phys. Rev. B* **51**, 9253 (1995).

[26] Andergassen, S. et al. Anomalous Isotopic Effect Near the Charge-Ordering Quantum Criticality. *Phys. Rev. Lett.* **87**, 056401 (2001).

[27] Perali, A., et al. d-wave superconductivity near charge instabilities. *Phys. Rev. B* **54**, 16216 (1996).

[28] Caprara, S., Grilli, M., Leridon, B., Vanacken, J. Parconductivity in layered cuprates behaves as if due to pairing of nearly free quasiparticles *Phys. Rev. B* **79**, 024506 (2009).

[29] Barišić, N., et al. Universal sheet resistance and revised phase diagram of the cuprate high-temperature superconductors. *Proc. Natl. Acad. Sci.* **110**, 12235 (2013).

[30] Cyr-Choinière, O., et al. Two types of nematicity in the phase diagram of the cuprate superconductor  $\text{YBa}_2\text{Cu}_3\text{O}_y$ . *Phys. Rev. B* **92**, 224502 (2015).

[31] Grbić, M. S., et al. Temperature range of superconducting fluctuations above  $T_c$  in  $\text{YBa}_2\text{Cu}_3\text{O}_{7-\delta}$  single crystals. *Phys. Rev. B* **83**, 144508 (2011).

[32] Ament, L. J. P., et al. Resonant inelastic x-ray scattering studies of elementary excitations. *Rev. Mod. Phys.* **83**, 705 (2011); Comin, R. & Damascelli, A. Resonant X-Ray Scattering Studies of Charge Order in Cuprates *Annu. Rev. Condens. Matter Phys.* **7**, 369 (2016).

[33] Gerber, S., et al. Three-dimensional charge density wave order in  $\text{YBa}_2\text{Cu}_3\text{O}_{6.67}$  at high magnetic fields. *Science* **350**, 949 (2015).

[34] Bluschke, M., et al. Stabilization of three-dimensional charge order in  $\text{YBa}_2\text{Cu}_3\text{O}_{6+x}$  via epitaxial growth. *Nat. Commun.* **9**, 2978 (2018).

[35] Caprara, S., Di Castro, C., Seibold, G., & Grilli, M. Dynamical charge density waves rule the phase diagram of cuprates. *Phys. Rev. B* **95**, 224511 (2017).

[36] Mazza, G., Grilli, M., Di Castro, C. & Caprara, S.

Evidence for phonon-like charge and spin fluctuations from an analysis of angle-resolved photoemission spectra of  $\text{La}_{2-x}\text{Sr}_x\text{CuO}_4$  superconductors. *Phys. Rev. B* **87**, 014511 (2013).

[37] Landauer, R., Electrical Transport and Optical Properties of Inhomogeneous Media, Garland, J. C. & Tanner, D. B. editors, 1978 (New York: AIP) p. 2; Kirkpatrick, S. Percolation and conduction. *Rev. Mod. Phys.* **45**, 574 (1973)

[38] G. Seibold et al., in preparation.